nature materials

ARTICLES

PUBLISHED ONLINE: 4 DECEMBER 2011 | DOI: 10.1038/NMAT3184

High electrochemical activity of the oxide phase in model ceria–Pt and ceria–Ni composite anodes

William C. Chueh†‡, Yong Hao†, WooChul Jung and Sossina M. Haile*

Fuel cells, and in particular solid-oxide fuel cells (SOFCs), enable high-efficiency conversion of chemical fuels into useful electrical energy and, as such, are expected to play a major role in a sustainable-energy future. A key step in the fuel-cell energy-conversion process is the electro-oxidation of the fuel at the anode. There has been increasing evidence in recent years that the presence of CeO_2-based oxides (ceria) in the anodes of SOFCs with oxygen-ion-conducting electrolytes significantly lowers the activation overpotential for hydrogen oxidation. Most of these studies, however, employ porous, composite electrode structures with ill-defined geometry and uncontrolled interfacial properties. Accordingly, the means by which electrocatalysis is enhanced has remained unclear. Here we demonstrate unambiguously, through the use of ceria–metal structures with well-defined geometries and interfaces, that the near-equilibrium H_2 oxidation reaction pathway is dominated by electrocatalysis at the oxide/gas interface with minimal contributions from the oxide/metal/gas triple-phase boundaries, even for structures with reaction-site densities approaching those of commercial SOFCs. This insight points towards ceria nanostructuring as a route to enhanced activity, rather than the traditional paradigm of metal-catalyst nanostructuring.

For SOFCs based on oxygen-ion (vacancy) conductors, the global anode reaction for hydrogen electro-oxidation is given by

$$H_2(g) + O_O^x \rightarrow H_2O(g) + V_O^{\bullet\bullet} + 2e'$$

where Kröger–Vink notation is used and $V_O^{\bullet\bullet}$ represents a doubly ionized oxygen vacancy, the majority ionic carrier. The anodes of typical SOFCs are porous composites formed of the electrolyte material and a catalytically active metal, most commonly Ni (ref. 1). It is generally accepted that the electrochemical reaction occurs within the composite structure in the near vicinity of the triple-phase boundaries (3PBs) at which the gas, electrolyte and metal phases are in simultaneous contact because of the requirement that each species—gas-phase molecules, oxygen ions (or vacancies) and electrons—be transported either to or from the reaction site; only at such boundaries are pathways for all three species accessible.

In recent years it has been increasingly common to include ceria as a component in SOFC anodes, whether as a functional inter-layer, as an impregnated catalyst or as the predominant oxide phase[1–8]. Many of the efforts are directed towards the development of coking-resistant and sulphur-tolerant anodes for direct operation of SOFCs on hydrocarbon fuels[9,10]. The effectiveness of ceria for methane electro-oxidation has been loosely connected to its exceptional oxygen-storage capacity, a trait that also renders it useful as an active support in non-electrochemical catalytic applications[11–14]. In the context of hydrogen electro-oxidation, most (but not all) studies find improvements on incorporation of ceria, relative to anodes based on yttria-stabilized zirconia[1,6–8,15,16] (YSZ). As ceria is a mixed ionic and electronic conductor under the reducing conditions of the anode[15,17–19], the ceria/gas interface is inherently accessible to both carriers. Thus, some or all of the double-phase boundary (2PB) can plausibly host electrocatalysis, and this feature has been suggested by some authors to be the source of enhanced electrocatalytic activity[1,19–27]. Indeed, direct interrogation of the Ce oxidation state at the electrode/gas interface using ambient-pressure X-ray photoelectron spectroscopy revealed an active reaction zone that extends as much as 150 μm from the gold current collector on the surface of columnar, undoped ceria thin films[27].

Despite the growing evidence for the high activity of ceria for direct fuel electro-oxidation at the ceria/gas interface, unequivocal elucidation of electrochemical reaction pathways in ceria-based electrodes has been hindered by the use of ill-defined microstructures and uncontrolled interfacial properties. It is not possible to assess, for example, whether the observed variation in overpotentials in Ni–ceria anodes with increasing Ni content[28] occurs because of variations in the Ni connectivity as proposed, or because of changes in the specific surface area or interfacial chemistry of ceria due to differences in processing conditions. Similarly, it is unclear whether the increases in activity observed on impregnation of ceria-based anodes with Pd (refs 5,29), Ni (ref. 30) or Ru (ref. 31) nanoparticles are directly due to the metals or due to changes in the oxide microstructure or surface characteristics. Experiments in which ceria is impregnated into Ni–YSZ anodes and improvements observed suffer from similar ambiguities. Even the large active reaction zone reported previously does not inherently demonstrate high surface activity, but may reflect high electronic conductivity instead[27].

Here, an unambiguous assessment of the relative activities of the 3PB and 2PB sites in ceria–metal structures is enabled by the use of well-defined geometries and interfaces (Fig. 1a). Patterned metal electrodes on solid-oxide electrolytes have revealed important aspects of hydrogen electrocatalysis at the Pt/YSZ and Ni/YSZ interfaces[32–35]. Here, 150–400-nm-thick Pt and Ni pattern strips, 5–120 μm in width and inter-metal spacings of similar values, were fabricated by photolithography on ~1-μm-thick films of $Sm_{0.2}Ce_{0.8}O_{1.9-\delta}$ (samaria-doped ceria, or SDC), in turn, obtained by pulsed laser deposition (PLD) on (100) single-crystal YSZ. Both the oxide and metal films exhibited excellent adhesion properties. The nominal, metal-catalysed (3PB) area-specific reaction-site

Materials Science, California Institute of Technology, Pasadena, California 91125, USA. †These authors contributed equally to this work. ‡Present address: Sandia National Laboratories, Livermore, California 94551, USA. *e-mail: smhaile@caltech.edu.

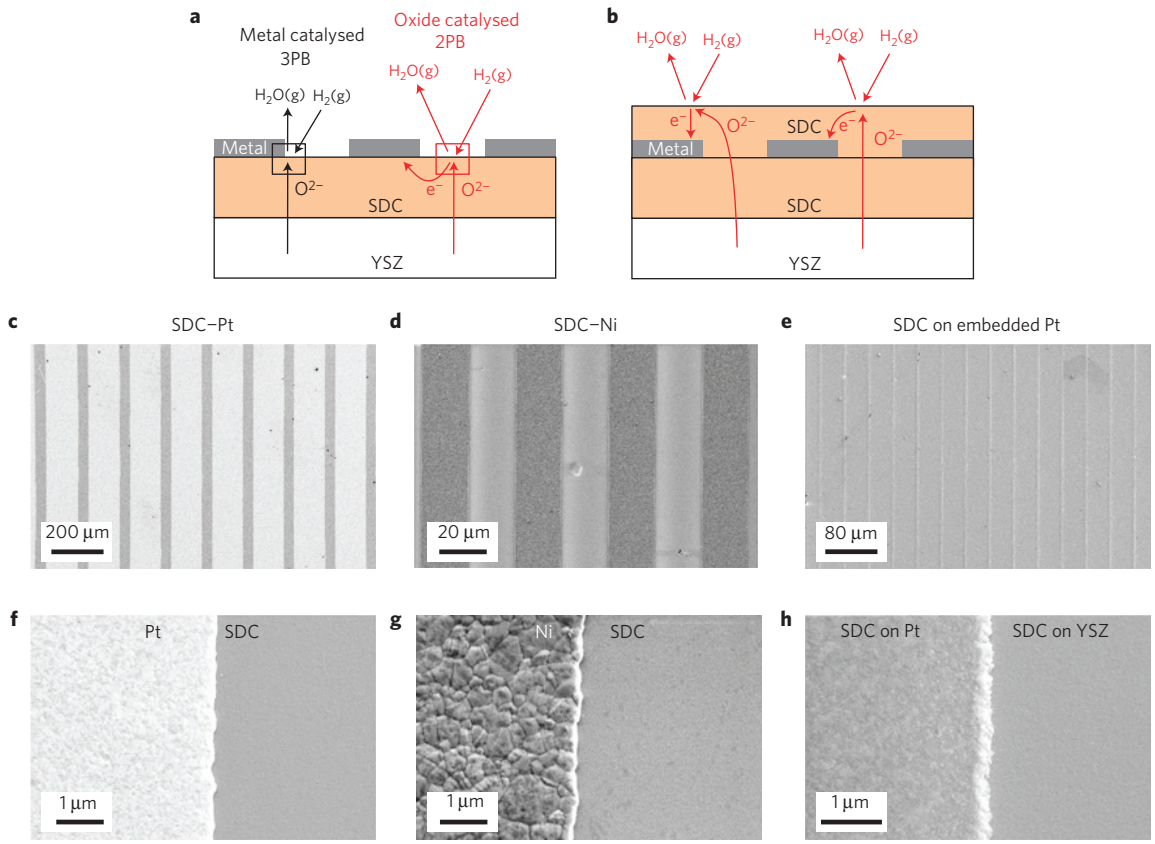

Figure 1 | Patterned metal on thin-film ceria as a model system to study competing electrochemical reactions. a, Schematic depicting the two macroscopic reaction sites present in a ceria–metal patterned electrode and the corresponding surface reaction and bulk diffusion steps. Bulk pathways involving the metal are not shown. **b**, Patterned electrode with an embedded current collector that eliminates contribution from the metallic phase. **c**–**h**, Planar SEM images of corresponding electrode structures, recorded after electrochemical characterization under H_2–H_2O–Ar atmospheres at 650 °C. (SDC = $Sm_{0.2}Ce_{0.8}O_{1.9-\delta}$, YSZ = $Y_{0.16}Zr_{0.84}O_{1.92}$.)

density, d_{3PB}, ranged from 1.3×10^2 to 2.0×10^3 cm^{-1} and the ceria-catalysed (2PB) reaction-site density, d_{2PB}, from 0.06 to 0.75 (Supplementary Table S1). Thus, a maximum d_{3PB} to d_{2PB} ratio of $\sim 4 \times 10^3$ cm^{-1}, comparable to those of composite electrodes used in commercial SOFCs, typically around 2×10^4 cm^{-1} (ref. 36) was attained in a model configuration. A modified geometry, with embedded Pt current collectors, was additionally employed to directly probe the ceria surface activity in the absence of 3PBs (Fig. 1b).

Suitability of films for electrochemical studies

Bulk chemical analysis by electron probe methods established that thin-film composition was identical, within error, to that of the PLD target. In-plane and out-of-plane X-ray diffraction analyses revealed that the films were epitaxial to the substrate (Supplementary Fig. S1a–c) with an out-of-plane lattice constant of 5.441 Å, comparable to that of bulk samples (5.433 Å; ref. 37). Cross-sectional transmission electron microscopy and selective area diffraction further confirmed the epitaxial nature of the film (Supplementary Fig. S1d), although the bulk-like value of the lattice constant in the film indicates negligible strain. In the vicinity of the SDC/YSZ interface, the electron diffraction pattern shows only the presence of peaks due to SDC and YSZ (Supplementary Fig. S1e), indicating the absence of a second phase at the interface, even after an additional annealing step at 900 °C for 20 h. This result is further supported by high-spatial-resolution chemical analysis across the substrate/film interface, which did not reveal detectable levels of cation inter-diffusion.

As shown in Fig. 1, in-plane electron migration is a key step in the reaction pathways and for this reason must be assessed. The in-plane conductivity, measured for SDC grown on YSZ (see Supplementary Information for details), was found to show the characteristic electrolytic and mixed conducting regimes typical of trivalent-doped ceria exposed to moderately reducing conditions. The total conductivity can be expressed as $\sigma_{tot} = \sigma_{ion} + \sigma_{eon}(p_{O_2})$, where the subscripts 'ion' and 'eon' indicate ionic and electronic partial conductivity, respectively. The ionic conductivity, measured under $p_{O_2} = 0.21$ atm, is comparable to that reported for bulk materials[38] (Supplementary Fig. S2a). Subtraction of this ionic component from the total conductivity yields the electronic contribution (Supplementary Fig. S2b). The expected $p_{O_2}^{-1/4}$ dependence[15,19,39] is clearly observed. Furthermore, the temperature dependence between 550 and 650 °C implies an activation energy of ~2.48 eV, comparable to those of microcrystalline materials (2.30 eV; ref. 38), shown alongside the present results in Supplementary Fig. S2c, whereas the absolute value of the electronic conductivity is also in reasonable agreement with literature values. Moreover, as reported previously[40], the Ce^{3+} to Ce^{4+} oxidation enthalpy and entropy for similarly prepared epitaxial films match closely with bulk values[41]. Thus, the films exhibit bulk-like characteristics, serving as appropriate representatives of ceria in microcrystalline, composite anode electrodes.

Essential to a study involving patterned electrodes is that the pattern features remain fixed over the course of the measurement. Images of the patterned films obtained after electrochemical characterization ($T_{max} = 650$ °C, $p_{H_2,max} = 0.13$ atm; Fig. 1c,d,f,g) show that indeed the patterned metals remain intact and retain sharply defined edge features. Despite grain growth in the metal

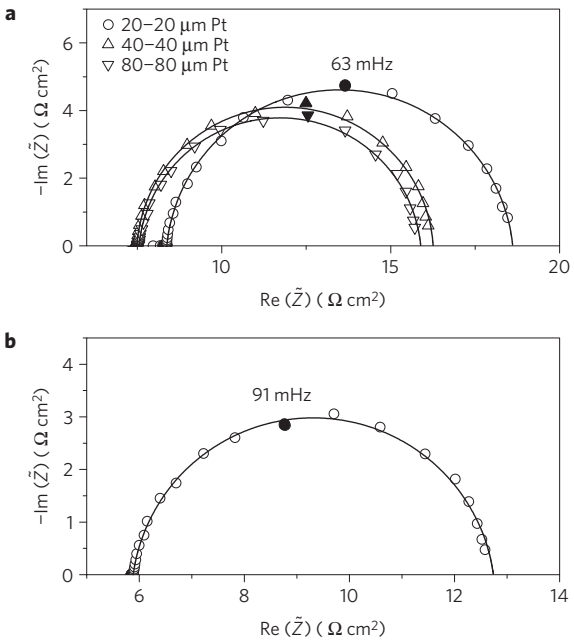

Figure 2 | Typical impedance spectra obtained from ceria–metal patterned electrodes presented in Nyquist form. a,**b**, Spectra are collected at 650 °C from electrochemical cells with Pt patterns on top of ceria thin film (**a**) and with an embedded Pt current collector sandwiched between two ceria thin-film layers (**b**). The solid lines represent fits. $p_{H_2} = 0.13$ atm and $p_{H_2O} = 0.0057$–0.0058 atm.

film (particularly noticeable in Ni), increases in the metal-feature perimeter were minimal, and, similarly, the formation of macroscopic pores was essentially negligible. The slight microstructural evolution detected is accounted for by reporting quantities relative to the actual dimensions of the Pt or Ni features and the surface area of the SDC films, as determined from image analysis (Supplementary Table S1). As might be expected, the embedded current collectors retained even greater structural integrity over the course of the measurement. It was found that the SDC deposited over Pt exhibited a dense, columnar morphology distinct from the featureless morphology over YSZ (Figs 1e,h and Supplementary Fig. S1f). The r.m.s. roughness after electrochemical characterization (Supplementary Fig. S3) was slightly greater over Pt than YSZ (1.9 versus 1.4 nm), but is considered sufficiently similar to have minimal impact on electrochemical behaviour. The overall low roughness justifies equating the 2PB reaction area with the projected area, given the comparable planar feature size. Additional imaging of the SDC deposited over Pt, achieved through focused ion beam cross-sectioning and *in situ* scanning electron microscopy (SEM), revealed the oxide overlayer to be free of detectable porosity (Supplementary Fig. S4), where, again, the imaging was carried out after electrochemical characterization. Beyond morphological features, it is also critical for such a study that the surface chemistry be well characterized. Using Auger electron spectroscopy, both the metal and SDC regions in the cells with metal exposed were found, after electrochemical measurements, to be free of macroscopic surface inter-diffusion (beyond 1 μm), Supplementary Fig. S5, whereas the 3PB regions, as examined by transmission electron microscopy (Supplementary Fig. S6), showed no surface impurity phases or, within detection limits, enhancement of surface impurities. Similarly, the SDC surface of the cell with an embedded current collector was found to be free of Pt, as probed by X-ray photoelectron spectroscopy after electrochemical characterization. Si was the only impurity element detected, with the cation fraction of the order of 0.2.

Electrochemical behaviour

For samples with metal features on top of SDC film, the zero-bias impedance response (Fig. 2a), plotted in Nyquist form, always consisted of one nearly perfect semi-circle, displaced from the origin by the YSZ ionic resistance as well as the current collector sheet resistance, where the arc reflects the characteristics of the electrochemical reaction and the SDC film. As shown elsewhere for similarly thick SDC films but with porous paste electrodes, the large capacitance response, ranging from 0.021 to 0.32 F cm^{-2}, is dominated by the chemical capacitance of the mixed conductor[40]. The resistance, as further supported by the gas-atmosphere dependence presented below, is dominated by an electrochemical process that occurs on the external surface, as might be expected given the epitaxial and impurity-free nature of the SDC/YSZ internal interface. Furthermore, the absence of a Warburg-like diffusion response implies that in-plane electron migration (from the ceria-catalysed reaction sites to the metal) is not rate-limiting[42]. The impedance response of the cell with embedded metal exhibited features identical to those of the cells with exposed current collectors (Fig. 2b).

On varying the metal-catalysed reaction-site (3PB) density by a factor of 16 while holding the ceria-catalysed reaction-site (2PB) density constant, it was observed that the electrochemical activity remains essentially unchanged and is moreover independent of the choice of metal (Fig. 3a,b). Here the electrochemical reaction resistance normalized to the total cell area is plotted versus 3PB density. The same behaviour was observed across a wide range of hydrogen and water vapour partial pressures. In the double-logarithmic plots a slope of 1 would indicate either that the reactions occur preferentially on the metal-catalysed sites or that lateral electron diffusion is rate-limiting; the observed slope -0.13 ± 0.06 for ceria–Pt and $+0.1 \pm 0.3$ for ceria–Ni (averaged under all conditions examined, see Supplementary Table S2) indicates that the reactions occur on the ceria-catalysed sites, with minimal contributions from the metal catalysts at the reaction-site densities probed and with negligible diffusion overpotential. The similarity in the absolute values for reaction resistance between Ni and Pt further supports the conclusion that the 3PBs contribute minimally to the overall reaction rate. Moreover, whereas it is largely independent of 3PB site density, the electrochemical reaction resistance exhibited a strong dependence on gas-phase composition. The nature of this dependence is similar between the Ni and Pt samples, indicating similar mechanistic pathways and further supporting the proposition of a reaction that occurs predominantly on the ceria surface.

In contrast to the metal-catalysed reaction-site density, the ceria-catalysed reaction-site density has a clear impact on global electrode activity. The double-logarithmic plots of area-specific electrode resistance versus 2PB site density (at constant 3PB site density) in Fig. 3c,d reveal average slopes of 1.0 ± 0.3 for Pt and 1.2 ± 0.3 for Ni (see Supplementary Table S2 for sample details), consistent with the behaviour expected for reactions that occur over the ceria/gas interface. This particular result further demonstrates that the predominant reaction pathway does not involve the metal patterns directly, that is, through mechanisms such as diffusion of adsorbates along the vertical grain boundaries of the metal thin films, surface adsorption followed by diffusion on the metal towards the 3PB, or reactions on any unintentional 3PB sites created by pin holes that cannot be imaged by SEM. Were the pathway to involve the patterned metal, the activity would be expected to be proportional to the area of the metal, and a slope of -1 would be expected in the double-logarithmic plot.

Scatter in the data in Fig. 3 is associated with the reproducibility of the SDC thin-film growth conditions. Within each deposition batch (up to four samples at a time), the variation in the measured

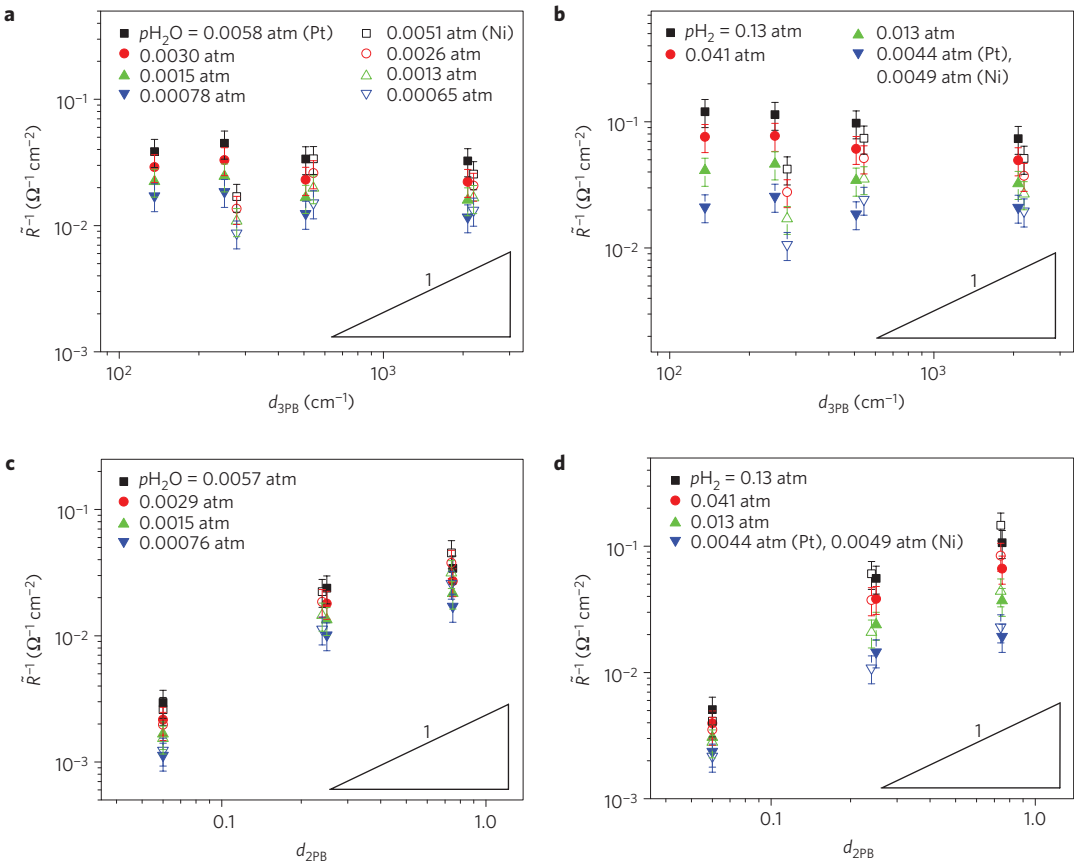

Figure 3 | Electrochemical activity in ceria–metal model electrodes. Filled symbols, Pt; open symbols, Ni. **a**–**d**, Activity as a function of the metal-catalysed, 3PB reaction-site density at 650 °C (with the nominal 2PB density held constant at 0.5) (**a**,**b**), and the ceria-catalysed, 2PB reaction-site density (with the nominal 3PB density held constant at 125 cm^{-1}) (**c**,**d**). $\tilde{R}$ represents resistance values normalized by the total electrode area. In **a**,**c**, the hydrogen partial pressure is held constant at 0.013 atm (Pt) and at 0.016 atm (Ni); in **b**, the water vapour pressure is held constant at ~0.0058 atm (Pt) and at ~0.0052 atm (Ni); in **d**, the water vapour pressure is held constant at ~0.0057 atm. Error bars indicate the variation in the electrode resistances of nominally identical ceria films deposited simultaneously.

resistance for nominally identical cells was found to be 25% (shown as error bars in Fig. 3), possibly owing to the variation in substrate temperature during growth. Batch-to-batch variation due to variable PLD conditions and impurity levels is expected to be greater. The slopes in the double-logarithmic plots are calculated using only samples from the same batch.

Turning to the results of the embedded-metal geometry (Fig. 4), it is apparent that the surface reaction resistances with and without 3PBs are almost identical. Here, the data for the exposed electrode configuration are normalized to the exposed ceria surface area (2PB site density) and only the results for the Pt samples, which exhibited less scatter than the Ni samples (and for which a greater number of measurements were carried out) are shown. In the absence of normalization for exposed ceria surface area, the embedded-metal geometry leads to a higher absolute activity, presumably due to its greater 2PB site density. The possibility that new, active and accessible 3PBs are created at the interface between the Pt and the SDC overlayer is remote owing to the high physical density of the deposited oxide. These results thus provide direct and conclusive evidence that the metal contributes minimally to the measured reaction rates under the conditions examined. Returning to the relationship between gas species and surface reaction rate, the data reveal a power-law dependence, p_{gas}^{n}, of electrode conductance on gas-phase partial pressure. The derived exponents are 0.4 for both hydrogen and water vapour in the case of the exposed electrode geometry (with error bars originating from the averaging of the data from Fig. 3), and are comparable to the values (0.3 for both gases) obtained for the embedded-metal geometry. Although relevant for assessing atomistic level mechanisms, elucidation of the origin of these exponents is beyond the scope of this work. Irrespective of mechanism and slight scatter in the data, the conclusion of predominant activity at the 2PBs remains.

In light of the quantitative determination of the surface interfacial reactivity and the electronic conductivity, it is possible to carry out a self-consistency check on the expected contribution of in-plane electronic diffusion to the measured resistance and to also estimate the extent of the electrochemical reaction zone. On the basis of the observation that the reaction is dominated by the surface reaction pathway, it can be concluded that sufficient in-plane electron diffusion occurs so as to facilitate reactions far away from the metal (which serves as the current collector) and, hence, the diffusion resistance must be small when compared with the surface resistance. At first glance this result is surprising given the low electronic conductivity of SDC (between 0.034 and 0.17 S cm^{-1} under the moderately reducing conditions examined). However, what establishes the significance of electron diffusion as a rate-limiting process is not the absolute electronic conductivity, but rather the relative magnitudes of the characteristic electron diffusion length, L_C, and the physical diffusion length (one-half of the inter-metal spacing). Approximating the lateral diffusion as a one-dimensional process, as justified by the low aspect ratio of the system, the characteristic diffusion length becomes $L_C = \sqrt{\sigma_{eon}\tilde{R}^{*}l}$, where σ_{eon} is the electronic conductivity, $\tilde{R}^{*}$ is the area-specific resistance of the ceria–gas reaction site and l

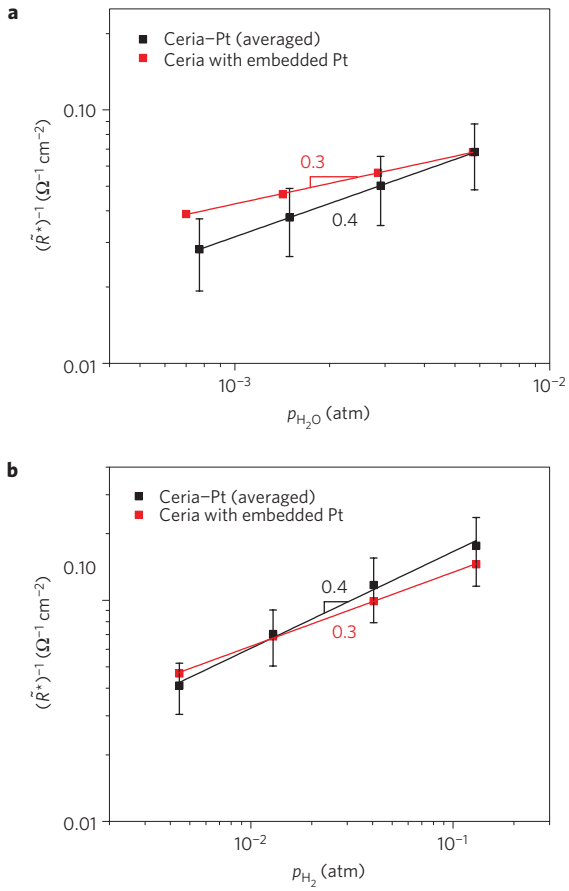

Figure 4 | Comparison of the electrochemical activity of ceria with and without metal 3PBs. a,**b**, Electrochemical activity for ceria–Pt cells with exposed metal features (average values of all data points shown in Fig. 3) and ceria–Pt–ceria cells with embedded metal current collectors at 650 °C as a function of water vapour pressure (with p_{H_2} held constant at 0.013 atm) (**a**) and as a function of hydrogen partial pressure (with p_{H_2O} held constant at ~0.0057 atm) (**b**). $\tilde{R}^*$ represents resistance values normalized by ceria/gas interfacial area. The error bars indicate the standard deviation of all measurements, ranging from 31 to 36%.

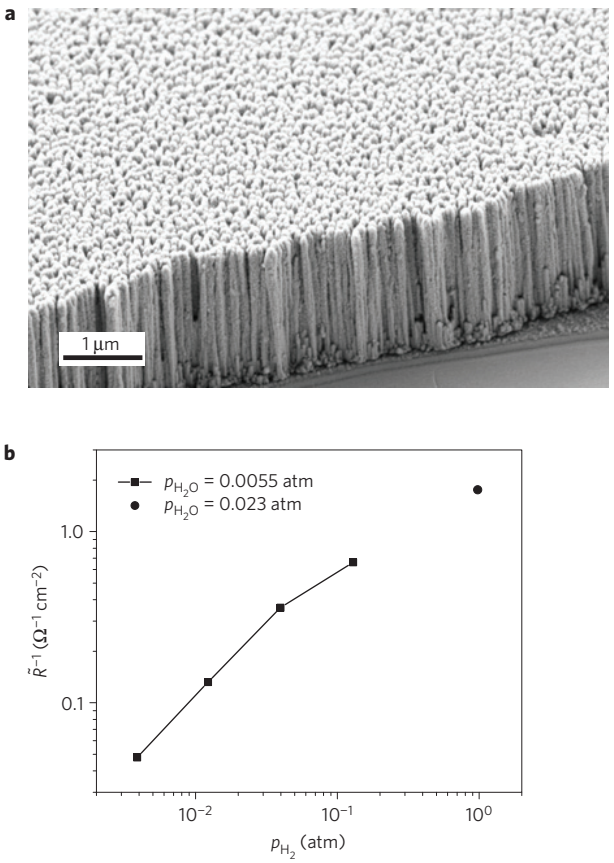

Figure 5 | Microstructural and electrochemical characteristics of a porous, columnar SDC electrode with a feature size of ~200 nm fabricated by PLD. a, Cross-sectional SEM micrograph (imaged before application of current collector). **b**, Inverse of total electrode resistance at 650 °C, normalized by the projected area, as a function of hydrogen partial pressure.

is the film thickness. The ratio of the physical diffusion length to the characteristic electron diffusion length, computed from experimentally measured parameters, is less than 1 under all conditions examined and attains a maximum value of 0.6 (for the sample with an inter-metal distance of 120 µm). Thus, despite the high surface activity, the SDC films employed in this work exhibit sufficiently high electronic conductivity such that reactions can occur considerably removed from the metal current collector with minimal diffusion overpotential.

Motivated by the possibility of attaining exceptionally high electrode activity simply by increasing the specific surface area of the oxide phase (total surface area per unit projected electrolyte area), we modified the film deposition conditions so as to grow nanostructured columnar SDC films (see Methods for details). Well-ordered columns with a width of ~200 nm were attained (Fig. 5a). To ensure that only the ceria activity contributed to the measured electrochemical response, gold current collectors with micrometre-sized grains were applied. Even with a relatively unoptimized current collection strategy (not all of the columns can easily be contacted), at 650 °C and under a humidified H_2 atmosphere (p_{H_2O} = 0.023 atm), an electrode resistance of just 0.60 Ω cm^2 was achieved from a ~2-µm-thick film (Fig. 5b and Supplementary Fig. S7). This level of activity exceeds the properties of the most promising of reported oxide anodes[43,44], despite the rather modest surface area enhancement achieved relative to a flat surface. Furthermore, preliminary investigations show that only ~0.36 Ω cm^2 of the total electrode resistance is, in fact, due to the surface electrochemical reaction (Supplementary Fig. S7), indicating a performance level approaching that of high-activity ceria–metal composite structures[45–47].

The combination of results presented here demonstrates unequivocally that ceria is inherently active towards hydrogen electro-oxidation and rationalizes the reports in the literature of higher fuel-cell power output when ceria is introduced into zirconia-based anodes, or completely replaces zirconia. The conclusions are furthermore in excellent qualitative agreement with our own previous studies[19,22], which led to the hypothesis that the metal-catalysed pathway does not contribute significantly to electrocatalysis (Supplementary Fig. S8). The observation by some authors that the introduction of metal nanoparticles into ceria-based anodes with moderate oxide surface area enhances activity is not inconsistent with the supposition of inherently high reaction rates on ceria. It can be concluded that some metals indeed catalyse the electro-oxidation on the ceria surface, and, when applied as nanoparticles, the number density of reaction sites can be substantially greater than the 3PB site densities examined here, such that the catalyst particles contribute significantly to lowering overpotentials. However, for those electrode structures in which both the ceria oxide phase and the metallic phase are nanostructured, the relative reaction-site density (d_{3PB} to d_{2PB}

ratio) is unlikely, particularly after high-temperature operation, to substantially exceed the highest values used in this work (4×10^3 cm^{-1}), and the role of the nanoparticulate metals in achieving the observed high activity[45,46] may be surprisingly small. Composite ceria electrode structures are further distinguished from traditional electrodes relying on 3PB-catalysed electrochemical reactions in that the metallic phase need not be contiguous because the mixed conducting oxide facilitates the electron transport.

Recognition of the important role of active oxides for fuel electrocatalysis provides guidance for the design and fabrication of fuel-cell anodes with exceptional performance. Nanostructuring of the ceria oxide component, to enhance the 2PB area, may be equally or more important than nanostructuring of metal catalysts to enhance the 3PB length. Inherent thermal and redox stability of ceria nanostructures further adds to their potential as fuel-cell anodes. Although the specific configurations demonstrated here may not, for a host of potential reasons, reflect truly commercially relevant geometries, the result is clear: even in the absence of metal catalysts, ceria-based electrodes can be expected to deliver substantial power densities.

Methods

Materials. Electrochemical cells with symmetric electrodes, with either exposed or embedded metal features, were fabricated on both sides of 10×10 mm $\times$ 0.5 mm (100) $Y_{0.16}Zr_{0.84}O_{1.92}$ (MTI) single crystals, which served as the oxygen-ion-conducting solid electrolyte. Thin-film $Sm_{0.2}Ce_{0.8}O_{1.9-\delta}$ electrodes with a typical thickness of 1 μm were grown by PLD (Neocera, with a Coherent 102 KrF 248 nm excimer laser, ~2 J cm^{-2}, 20 Hz). The PLD targets were compacted from high-purity commercial SDC powder (Nextech Materials) at 350 MPa using an isostatic press and sintered at 1,250 °C for 5 h. To avoid contamination, sacrificial layers, also YSZ, were placed between the substrate and the PLD heater stage. The growth temperature, measured by a thermocouple in direct contact with the YSZ wafer (bonded with Pt adhesive paste), was ~650 °C. Average heating rates were 7 °C min^{-1}. The deposition atmosphere was pure oxygen (5–20 mtorr). After deposition of the second side was completed, all samples were annealed in oxygen (100 torr) for 1 h in the PLD chamber at ~650 °C.

Metal patterns (joined by a 1-mm-wide metal border) were fabricated by metal liftoff photolithography. First, a positive photoresist (Shipley 1813) was spin-coated onto YSZ substrates at 2,000–3,000 r.p.m., and baked at 115 °C for 150 s. Next, a glass mask plate metallized by chromium and with defined patterns was aligned with the samples in a contact aligner (Karl Suss MJB 3) and exposed to ultraviolet light for 45–75 s. The samples were then immersed in Microposit MF-319 solution for ~30–60 s to develop the photoresist. After rinsing by deionized water and drying, the samples were cleaned using an oxygen plasma to remove residual organics and then transferred to a d.c. magnetron sputtering system (AJA International) where Pt (99.99% purity) or Ni (99.999% purity) was deposited atop the photoresist layer. Ar pressure during film growth was 3 mtorr. Growth rates were approximately 10 and 7 nm min^{-1} for Pt and Ni, respectively. Deposited current collectors were typically 150–200 nm thick for Pt and 300–400 nm thick for Ni. Metal liftoff was carried out by immersing the samples in acetone at room temperature. The above procedure was repeated for the other side of the substrate. For cells with embedded metal patterns, the patterned samples were first annealed in various H_2–H_2O–Ar atmospheres at 650 °C to eliminate microstructural evolution during subsequent second-layer ceria deposition (0.9 μm thick). Experiments were carried out specifically using a Pt pattern with metal strips 5 μm in width and spaced 35 μm apart. A relatively narrow metal line (5 μm) width is used to minimize the in-plane ionic transport distance and prevent a diffusion gradient from developing.

Symmetric cells with porous SDC electrodes were also prepared by PLD on YSZ single-crystal electrolytes (~2 J cm^{-2}, 20 Hz, 90 mtorr O_2, ~650 °C). After annealing in oxygen (100 torr) for 20 min in the PLD chamber at ~650 °C, the cell was cooled and Ar sputtered (AJA International, 3 mtorr, 50 W) for 80 min per side at room temperature, to improve contact with the current collector. Finally, Au paste (Nextech Materials Au-I-10) was applied by brush-painting and subsequently annealed at 700 °C for 2 h in stagnant air.

Methods. Electrode activity was characterized by electrochemical impedance spectroscopy under controlled temperatures and atmospheres. Before electrochemical measurements, the completed cells were cleaned by rinsing and soaking in acetone, isopropanol, deionized water and methanol, and dried by ultrahigh-purity compressed helium. The samples were then placed inside a continuous-flow alumina tube (20 mm inner diameter) to which H_2–H_2O–Ar was delivered through digital mass flow controllers, with some of the gas passed through a water bubbler placed inside an isothermal water bath. The total flow rate was kept constant at 101 cm^3 min^{-1} (standard temperature and pressure). Effluent humidity was monitored using a Rotronic Hygroflex capacitive sensor. Impedance measurements were made using a Solartron 1260A frequency response analyser at a zero bias with a perturbation amplitude of 20 mV. A four-probe configuration was used to minimize inductance effects from the wiring. All measurements were carried out at 650 °C and initial heating was carried out under a low hydrogen partial pressure to minimize incorporation of interstitial hydrogen into the metal. For the patterned dense electrodes, the gas partial pressures were limited to 0.13 atm (H_2) and 0.006 atm (H_2O) to avoid ceria film cracking due to chemical expansion and to minimize water-vapour-driven impurity segregations. Both the post-characterized metal and oxide films remained adhered to the substrate when pulled on using either Scotch or carbon tape. See Supplementary Information for details on physical and chemical characterizations.

Received 1 April 2011; accepted 26 October 2011; published online 4 December 2011

References

1. Jiang, S. P. & Chan, S. H. A review of anode materials development in solid oxide fuel cells. *J. Mater. Sci.* **39,** 4405–4439 (2004).
2. Sholklapper, T. Z., Kurokawa, H., Jacobson, C. P., Visco, S. J. & De Jonghe, L. C. Nanostructured solid oxide fuel cell electrodes. *Nano Lett.* **7,** 2136–2141 (2007).
3. Kurokawa, H., Sholklapper, T. Z., Jacobson, C. P., De Jonghe, L. C. & Visco, S. J. Ceria nanocoating for sulfur tolerant Ni-based anodes of solid oxide fuel cells. *Electrochem. Solid State* **10,** B135–B138 (2007).
4. Gorte, R. J. & Vohs, J. M. Nanostructured anodes for solid oxide fuel cells. *Curr. Opin. Colloid Interface* **14,** 236–244 (2009).
5. Gross, M. D., Vohs, J. M. & Gorte, R. J. A strategy for achieving high performance with SOFC ceramic anodes. *Electrochem. Solid State* **10,** B65–B69 (2007).
6. Marina, O. A., Bagger, C., Primdahl, S. & Mogensen, M. A solid oxide fuel cell with a gadolinia-doped ceria anode: Preparation and performance. *Solid State Ion.* **123,** 199–208 (1999).
7. Tsai, T. & Barnett, S. A. Increased solid-oxide fuel cell power density using interfacial ceria layer. *Solid State Ion.* **98,** 191–196 (1997).
8. Tsai, T. & Barnett, S. A. Effect of mixed-conducting interfacial layers on solid oxide fuel cell anode performance. *J. Electrochem. Soc.* **145,** 1696–1701 (1998).
9. Murray, E. P., Tsai, T. & Barnett, S. A. A direct-methane fuel cell with a ceria-based anode. *Nature* **400,** 649–651 (1999).
10. Park, S., Vohs, J. M. & Gorte, R. J. Direct oxidation of hydrocarbons in solid-oxide fuel cell. *Nature* **404,** 265–267 (2000).
11. Fu, Q., Weber, A. & Flytzani-Stephanopoulos, M. Nanostructured Au–CeO_2 catalysts for low-temperature water-gas shift. *Catal. Lett.* **77,** 87–95 (2001).
12. Park, J. B. *et al.* High catalytic activity of Au/CeO_x/TiO_2(110) controlled by the nature of the mixed-metal oxide at the nanometer level. *Proc. Natl Acad. Sci. USA* **163,** 4975–4980 (2009).
13. Rodriguez, J. A. *et al.* Activity of CeO_x and TiO_x nanoparticles grown on Au(111) in the water–gas-shift reaction. *Science* **318,** 1757–1760 (2007).
14. Trovarelli, A. Catalytic properties of ceria and CeO_2-containing materials. *Catal. Rev. Sci. Eng.* **38,** 439–520 (1996).
15. Eguchi, K., Setoguchi, T., Inoue, T. & Arai, H. Electrical properties of ceria-based oxides and their application to solid oxide fuel cells. *Solid State Ion.* **52,** 165–172 (1992).
16. Setoguchi, T., Okamoto, K., Eguchi, K. & Arai, H. Effects of anode material and fuel on anodic reaction of solid oxide fuel cells. *J. Electrochem. Soc.* **139,** 2875–2880 (1992).
17. Ruiz-Trejo, E. & Maier, J. Electronic transport in single crystals of Gd-doped ceria. *J. Electrochem. Soc.* **154,** 583–587 (2007).
18. Tuller, H. L. & Nowick, A. S. Small polaron electron-transport in reduced CeO_2 single-crystals. *J. Phys. Chem. Solids* **38,** 859–867 (1977).
19. Lai, W. & Haile, S. M. Impedance spectroscopy as a tool for chemical and electrochemical analysis of mixed conductors: A case study of ceria. *J. Am. Ceram. Soc.* **88,** 2979–2997 (2005).
20. Lu, C., Worrell, W. L., Vohs, J. M. & Gorte, R. J. A comparison of Cu-ceria-SDC and Au-ceria-SDC composites for SOFC anodes. *J. Electrochem. Soc.* **150,** A1357–A1359 (2003).
21. Lai, W. *Impedance Spectroscopy as a Tool for the Electrochemical Study of Mixed Conducting Ceria*. PhD thesis, California Inst. Technology, (2006).
22. Chueh, W. C., Lai, W. & Haile, S. M. Electrochemical behavior of ceria with selected metal electrodes. *Solid State Ion.* **179,** 1036–1041 (2008).
23. Ciucci, F., Chueh, W. C., Goodwin, D. G. & Haile, S. M. Surface reaction and transport in mixed conductors with electrochemically-active surfaces: A 2-D numerical study of ceria. *Phys. Chem. Chem. Phys.* **13,** 2121–2135 (2011).
24. DeCaluwe, S. C. *et al. In situ* characterization of ceria oxidation states in high-temperature electrochemical cells with ambient pressure XPS. *J. Phys. Chem. C* **114,** 19853–19861 (2010).
25. Nakamura, T. *et al.* Determination of the reaction zone in gadolinia-doped ceria anode for solid oxide fuel cell. *J. Electrochem. Soc.* **155,** 1244–1250 (2008).
26. Nakamura, T. *et al.* Electrochemical behaviors of mixed conducting oxide anodes for solid oxide fuel cells. *J. Electrochem. Soc.* **155,** 563–569 (2008).

27. Zhang, C. J. *et al.* Measuring fundamental properties in operating solid oxide electrochemical cells by using in situ X-ray photoelectron spectroscopy. *Nature Mater.* **9,** 944–949 (2010).
28. Chen, M., Kim, B. H., Xu, Q., Ahn, B. G. & Huang, D. P. Effect of Ni content on the microstructure and electrochemical properties of Ni-SDC anodes for IT-SOFC. *Solid State Ion.* **181,** 1119–1124 (2010).
29. McIntosh, S., Vohs, J. M. & Gorte, R. J. Effect of precious-metal dopants on SOFC anodes for direct utilization of hydrocarbons. *Electrochem. Solid State* **6,** A240–A243 (2003).
30. Uchida, H., Suzuki, S. & Watanabe, M. High performance electrode for medium-temperature solid oxide fuel cells: Mixed conducting ceria-based anode with highly dispersed Ni electrocatalysts. *Electrochem. Solid State* **6,** A174–A177 (2003).
31. Uchida, H., Osuga, T. & Watanabe, M. High-performance electrode for medium-temperature solid oxide fuel cells: Control of microstructure of ceria-based anodes with highly dispersed ruthenium electrocatalysts. *J. Electrochem. Soc.* **146,** 1677–1682 (1999).
32. Bessler, W. G. *et al.* Model anodes and anode models for understanding the mechanism of hydrogen oxidation in solid oxide fuel cells. *Phys. Chem. Chem. Phys.* **12,** 13888–13903 (2010).
33. Bieberle, A., Meier, L. P. & Gauckler, L. J. The electrochemistry of Ni pattern anodes used as solid oxide fuel cell model electrodes. *J. Electrochem. Soc.* **148,** A646–A656 (2001).
34. Mizusaki, J., Amano, K., Yamauchi, S. & Fueki, K. Electrode-reaction at $Pt,O_2(g)$/stabilized zirconia interfaces. Part II. Electrochemical measurements & analysis. *Solid State Ion.* **22,** 323–330 (1987).
35. Mizusaki, J. *et al.* Kinetic studies of the reaction at the nickel pattern electrode on YSZ in H_2–H_2O atmospheres. *Solid State Ion.* **70,** 52–58 (1994).
36. Wilson, J. R. *et al.* Three-dimensional reconstruction of a solid-oxide fuel-cell anode. *Nature Mater.* **5,** 541–544 (2006).
37. Brauer, G. & Gradinger, H. Uber heterotype Mischphasen bei Seltenerdoxyden. I. *Z. Anorg. Allg. Chem.* **276,** 209–226 (1954).
38. Godickemeier, M. & Gauckler, L. J. Engineering of solid oxide fuel cells with ceria-based electrolytes. *J. Electrochem. Soc.* **145,** 414–421 (1998).
39. Mogensen, M., Sammes, N. M. & Tompsett, G. A. Physical, chemical and electrochemical properties of pure an doped ceria. *Solid State Ion.* **129,** 63–94 (2000).
40. Chueh, W. C. & Haile, S. M. Electrochemical studies of capacitance in cerium oxide thin films and its relationship to anionic and electronic defect densities. *Phys. Chem. Chem. Phys.* **11,** 8144–8148 (2009).
41. Kobayashi, T., Wang, S., Dokiya, M., Tagawa, H. & Hashimoto, T. Oxygen nonstoichiometry of $Ce_{1-y}Sm_yO_{2-0.5y-x}$ ($y = 0.1, 0.2$). *Solid State Ion.* **126,** 349–357 (1999).
42. Chueh, W. C. *Electrochemical and Thermochemical Behavior of* CeO_{2-x}. PhD thesis, California Inst. Technology (2011).
43. Huang, Y-H., Dass, R. I., Xing, Z-L. & Goodenough, J. B. Double perovskite as anode materials for solid-oxide fuel cells. *Science* **312,** 254–257 (2006).
44. Tao, S. & Irvine, J. T. S. A redox-stable efficient anode for solid-oxide fuel cells. *Nature Mater.* **2,** 320–323 (2003).
45. Zha, S., Rauch, W. & Liu, M. Ni–$Ce_{0.9}Gd_{0.1}O_{1.95}$ anode for GDC electrolyte-based low-temperature SOFCs. *Solid State Ion.* **166,** 241–250 (2004).
46. Muecke, U. P. *et al.* Electrochemical performance of nanocrystalline nickel/gadolinia-doped ceria thin film anodes for solid oxide fuel cells. *Solid State Ion.* **178,** 1762–1768 (2008).
47. Primdahl, S. & Mogensen, M. Mixed conductor anodes: Ni as electrocatalyst for hydrogen conversion. *Solid State Ion.* **152–153,** 597–608 (2002).

Acknowledgements

This work was supported in part by the Stanford Global Climate & Energy Project and by the National Science Foundation under contract number DMR-0604004. Additional support was provided by the NSF through the Caltech Center for the Science and Engineering of Materials, a Materials Research Science and Engineering Center (DMR-052056). W.C.C. was also supported by an appointment to the Sandia National Laboratories Truman Fellowship in National Security Science and Engineering, sponsored by Sandia Corporation (a wholly owned subsidiary of Lockheed Martin Corporation) as Operator of Sandia National Laboratories under its US Department of Energy Contract No. DE-AC04-94AL85000. The authors also acknowledge C. M. Garland and D. A. Boyd of Caltech and M. W. Clift of Sandia for their assistance with analytical measurements, K. L. Gu of Caltech for sample fabrication, F. Ciucci of University of Heidelberg for numerical simulations and D. G. Goodwin and E. C. Brown of Caltech and F. El Gabaly and A. H. McDaniel of Sandia for valuable discussions. The Evans Analytical Group carried out focused ion beam imaging, and for that effort the authors are particularly grateful to H. Deng.

Author contributions

W.C.C. designed the experiment, fabricated samples and carried out analytical and electrochemical characterizations. Y.H. developed the fabrication methodology for dense electrochemical cells and carried out the sample preparations and characterizations. W.J. fabricated and characterized porous electrochemical cells. S.M.H. guided and supervised the work.

Additional information

The authors declare no competing financial interests. Supplementary information accompanies this paper on www.nature.com/naturematerials. Reprints and permissions information is available online at http://www.nature.com/reprints. Correspondence and requests for materials should be addressed to S.M.H.